Joule

CellPress

Article

Over 10 kg m^{-2} h^{-1} Evaporation Rate Enabled by a 3D Interconnected Porous Carbon Foam

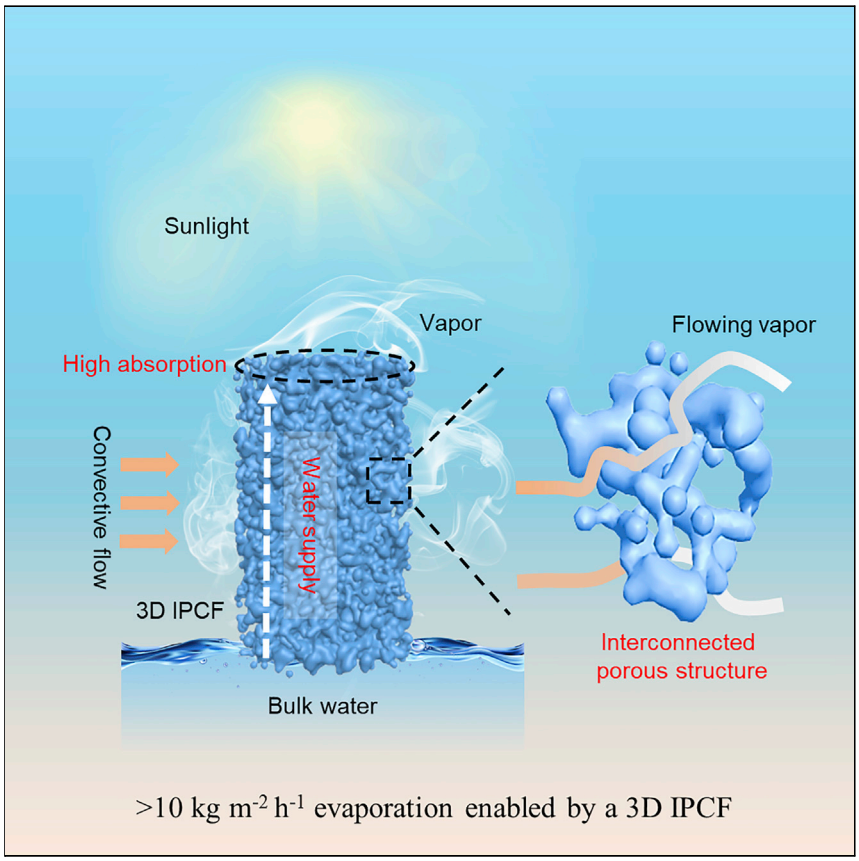

A three-dimensional (3D) interconnected porous carbon foam was developed. It is capable of not only effective phase transition but also vapor diffusion assisted by a convective flow. Therefore, evaporation rate as high as 10.9 kg m^{-2} h^{-1} is realized, which is highly desirable for evaporative water treatment technology.

Jinlei Li, Xueyang Wang, Zhenhui Lin, ..., Lin Zhou, Shining Zhu, Jia Zhu

jiazhu@nju.edu.cn

HIGHLIGHTS

A porous evaporator is tailored for effective phase transition and vapor diffusion

Unique gas-assisted expansion and perforation is developed for the evaporator

An evaporation rate of 10.9 kg m^{-2} h^{-1} is realized under 1 sun with a convective flow

High evaporation rate can be maintained day and night

Li et al., Joule 4, 1–10
April 15, 2020
https://doi.org/10.1016/j.joule.2020.02.014

Please cite this article in press as: Li et al., Over 10 kg m^{-2} h^{-1} Evaporation Rate Enabled by a 3D Interconnected Porous Carbon Foam, Joule (2020), https://doi.org/10.1016/j.joule.2020.02.014

Joule

CellPress

Article

Over 10 kg m^{-2} h^{-1} Evaporation Rate Enabled by a 3D Interconnected Porous Carbon Foam

Jinlei Li,[1,2] Xueyang Wang,[1,2] Zhenhui Lin,[1,2] Ning Xu,[1] Xiuqiang Li,[1] Jie Liang,[1] Wei Zhao,[1] Renxing Lin,[1] Bin Zhu,[1] Guoliang Liu,[1] Lin Zhou,[1] Shining Zhu,[1] and Jia Zhu[1,3,*]

SUMMARY

The recent advancements in evaporating water using renewable energy provide one of the promising pathways for treating water with minimized carbon footprint. Pursuing a high evaporation rate of water has been the central focus of this field, as it is directly related to the throughput of evaporative water treatment. However, in conventional designs of evaporators, diffusion of vapor into the atmospheric environment has been the limiting step for evaporation. In this work, we demonstrate that a carbon foam with a three-dimensional interconnected porous structure enables sufficient diffusion of vapor with a convective flow and therefore realizes an evaporation rate as high as 10.9 kg m^{-2} h^{-1} and outdoor evaporation of 42.0 kg m^{-2} for continuous 13 h. With such a high evaporation rate achieved, it shows great promise toward a high-throughput, around-the-clock, and eco-friendly technology of evaporative wastewater disposal.

INTRODUCTION

Over the past decades, the intensified consumption of clean water and severe pollution on the ecosystem have exposed human beings to an unprecedented urgency of the water crisis.[1–4] As water and energy pose as intertwined challenges, it is desirable to develop advanced water treatment technologies with minimized carbon footprint.[5,6] Among various pathways of water treatment, there is significant effort to evaporate water directly using renewable energy, such as solar energy.[7–27] For almost all the water treatments, such as wastewater disposal, noble metal recycling, and sea salt production, the throughput is the crucial parameter for practical applications, which calls for a high evaporation rate in the evaporative method.[7,28] Indeed, various porous evaporators have been developed to pursue this goal in the past few years.[7,9,11,29–33]

A close examination of the evaporation process within conventional porous evaporators reveals that evaporation rate is determined by two sequential steps, phase transition and diffusion.[34–37] In the first step of phase transition, water molecules come out of the evaporative surface to become vapor. In the second step of diffusion, the vapor diffuses out of porous structures to the atmospheric environment. Most of the previous efforts have focused on increasing the evaporative surface to maximize the first step of the phase transition. However, in conventional porous evaporators, a large amount of vapor gets stagnated within the pores due to insufficient diffusion. For porous structures with closed ends, vapor will be confined instead of diffusing out, restricting the evaporation rate (Figure 1A).

Context & Scale

Recently, evaporative water treatment driven by renewable energy is emerging as one of most promising approaches to address the growing water shortage with minimized carbon footprint. Pursuing a high evaporation rate is the central focus of this domain. Past advancements mainly rely on promoting the phase transition from water to vapor via tailoring structures at nano and/or microscale. In this work, we reveal that it is crucial to promote vapor diffusion to the environment. A three-dimensional (3D) interconnected porous carbon foam is designed to realize an evaporation rate as high as 10.9 kg m^{-2} h^{-1} under 1-sun illumination coupled with a natural convective flow. It is expected that the strategy reported here could open up a new path for developing high-throughput evaporative water treatment.

Please cite this article in press as: Li et al., Over 10 kg m^{-2} h^{-1} Evaporation Rate Enabled by a 3D Interconnected Porous Carbon Foam, Joule (2020), https://doi.org/10.1016/j.joule.2020.02.014

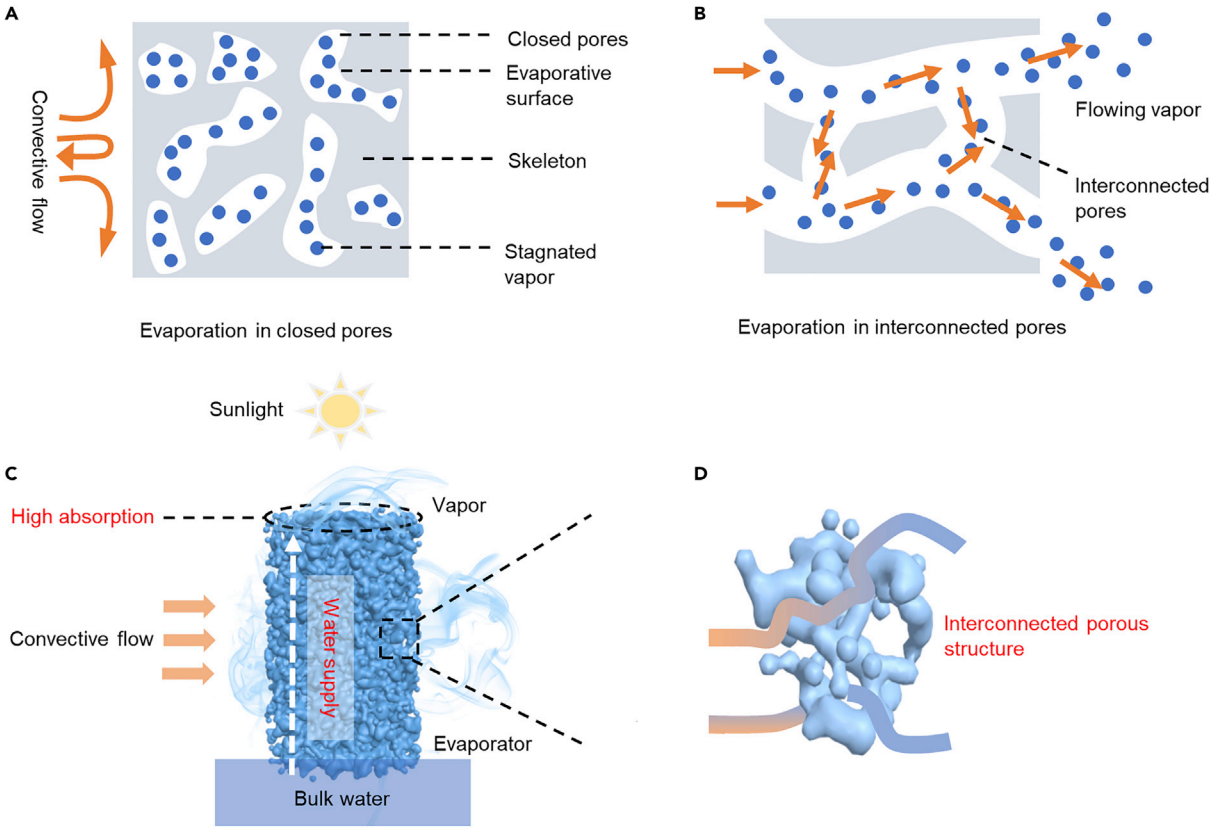

Figure 1. Schematics of Water Evaporation in a Conventional Evaporator and a 3D Interconnected Porous Evaporator

(A) A schematic of evaporation in a traditional evaporator, which is limited by weak diffusion of vapor within closed pores. Vapor generated from the evaporative surface stagnates within closed pores, resulting in ineffective diffusion and evaporation.

(B) A schematic of effective evaporation enabled by interconnected pores. The interconnected porous structure allows effective diffusion of vapor with a convective flow.

(C) A schematic shows the design concept of the 3D interconnected porous evaporator for realizing a high evaporation rate. Its 3D architecture provides ample evaporative surface for effective evaporation, excellent hydrophilicity for water supply, and high absorption of sunlight.

(D) A microscopic picture of the interconnected porous structure, which ensures effective vapor diffusion with a natural convective flow.

Therefore, it is essential to carefully tailor porous structures for both effective phase transition and vapor diffusion (Figure 1B), in addition to general considerations of optical and thermal management and water supply.[38] There are a few critical requirements for the designs of evaporators (Figure 1C). First of all, it should have a porous structure to provide ample evaporative surface. This porous structure should have excellent hydrophilicity, which ensures timely water supply. Most importantly, all the pores within the structures have to be interconnected to make sure effective vapor diffusion with a natural convective flow (Figure 1D). Finally, the pore size needs to be optimized, as there is a balance between the surface area for evaporation and space for effective diffusion, as explained in more detail below.

RESULTS AND DISCUSSION

Fabrication and Characterization of the Evaporator

This design of evaporators is achieved via unique gas-assisted expansion and perforation processes. As shown in Figure 2A, sucrose reacts with concentrated sulfuric acid in a cylinder quartz mold (more details in Experimental Procedures). In this step, sucrose is dehydrated by concentrated sulfuric acid to become carbon materials ($C_6H_{12}O_6 \rightarrow 6C + 6H_2O$) with high sunlight absorption and excellent hydrophilicity. Subsequently, part

[1]National Laboratory of Solid State Microstructures, College of Engineering and Applied Sciences, Jiangsu Key Laboratory of Artificial Functional Materials, Nanjing University, Nanjing 210093, P.R. China

[2]These authors contributed equally

[3]Lead Contact

*Correspondence: jiazhu@nju.edu.cn

https://doi.org/10.1016/j.joule.2020.02.014

Please cite this article in press as: Li et al., Over 10 kg m^{-2} h^{-1} Evaporation Rate Enabled by a 3D Interconnected Porous Carbon Foam, Joule (2020), https://doi.org/10.1016/j.joule.2020.02.014

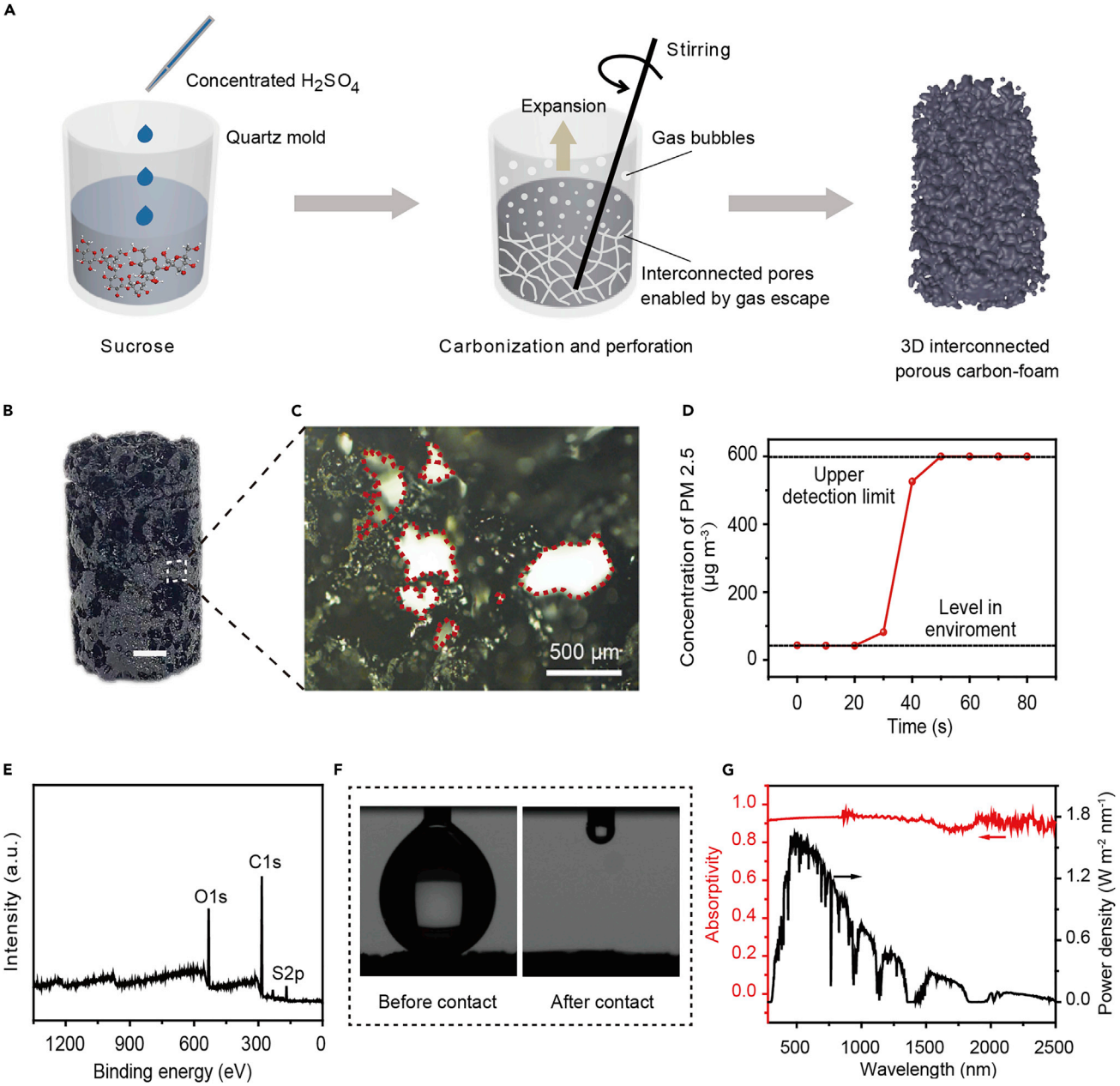

Figure 2. Fabrication and Characterizations of 3D IPCF

(A) The fabrication process of the 3D IPCF. Sucrose was carbonized by concentrated sulfuric acid and followed by unique gas-assisted expansion and perforation.

(B) A photograph of the 3D IPCF. Scale bar, 1 cm.

(C) Optical micrograph of the 3D IPCF. The sizes of these interconnected pores range from a few tens of micrometers to a few millimeters.

(D) PM2.5 is able to pass through the 3D IPCF over time. This indicates that the pores of the 3D IPCF are interconnected for convective flows with air molecules to pass through.

(E) XPS spectrum of the 3D IPCF indicates that it is made from carbon, oxygen, and sulfur.

(F) Water contact angle for the 3D IPCF, suggesting its super hydrophilicity, as water drop rapidly infiltrates into it.

(G) The optical absorption spectrum of the 3D IPCF and the spectrum of solar irradiation.

of carbon material reacts with concentrated sulfuric acid and generates gas mixtures ($C + 2H_2SO_4 \rightarrow CO_2\uparrow + 4SO_2\uparrow + 2H_2O$), leading to a huge volume expansion (up to 700%) and a three-dimensional (3D) structure. Meanwhile, as gas generated inside always tends

Please cite this article in press as: Li et al., Over 10 kg m^{-2} h^{-1} Evaporation Rate Enabled by a 3D Interconnected Porous Carbon Foam, Joule (2020), https://doi.org/10.1016/j.joule.2020.02.014

to escape to the ambient environment, it perforates the structure and ensures an interconnected porous structure from inside to the environment. As a result, a 3D interconnected porous carbon foam (3D IPCF) is fabricated.

As shown in Figure 2B, the as-prepared IPCF appears black and has a 3D porous structure. Its microstructures are presented in Figures 2C and S1, which clearly show that there are abundant and interconnected pores with diameters from tens of micrometers to a few millimeters. As discussed before, it is critical that these pores are interconnected. As direct evidence, it is found that particles less than 2.5 μm in diameter (PM.2.5) can continuously pass through the 3D IPCF (Figure 2D; see Figure S2 for more information). The X-ray photoelectron spectroscopy (XPS) spectrum in Figure 2E reveals that after carbonization, the main elemental components of the 3D IPCF are carbon, oxygen, and sulfur. The hydrophilic groups of C-O, C=O, and CSOx in the 3D IPCF (Figure S3) are beneficial for continuous water supply. Its excellent hydrophilicity can find direct evidence from the rapid water infiltration, as shown in Figure 2F. The absorptive spectrum of the 3D IPCF in Figure 2G indicates that it realizes 93% absorption for the global standard sunlight spectrum of AM 1.5 G[39,40] (nearly independent to pore size, Figure S4).

Dependence of Performance on Pore Size

As discussed above, the porous structure of the 3D IPCF is crucial for convective flow-assisted vapor diffusion. Herein, we first studied the dependence of the evaporation rate of the 3D IPCF on pore size. As shown in Figure 3A, we found that the 3D IPCFs with different pore sizes have similar evaporation rates of mere ~0.4 kg m^{-2} h^{-1} without convective flow (normalized by the projected area, similarly hereinafter) as it is limited by diffusion (see Figure S5 for the evaporative device). Strikingly, the evaporation rates of the 3D IPCFs with an average pore size of 5.8 (2.8) mm (Figure S6 for distribution of pore diameter) increase to 5.6 (4.6) kg m^{-2} h^{-1} with a convective flow of 2 m s^{-1} (a light breeze according to Beaufort Wind Scale[41]). For comparison, under the same convective flow, the evaporative performances of the 3D IPCFs with pore sizes of 150 and 350 μm are 3.2 and 3.8 kg m^{-2} h^{-1}, respectively. A similar trend of higher evaporation rate for larger pore size is observed under a convective flow of 6 m s^{-1} (moderate breeze). It is clear that the 3D IPCF with a larger pore size can enable more effective vapor diffusion by a convective flow, compared with that with small pore size (see Figure S7 for more evidence). This is contradictory to the traditional wisdom, in which highly porous structures with small pore size and high evaporative surface have been considered to be ideal for achieving a high evaporation rate. Hence, it is recognized that for the design of porous evaporators, it is essential to tailor the structures to match the rate of phase transition and diffusion rather than pursuing a high evaporative surface infinitely.

Subsequently, the evaporative behaviors of the 3D IPCFs under sunlight illumination (with incident angle of 90°) were studied carefully to verify the aforementioned relationships further. As presented in Figure 3B, the 3D IPCFs with different pore sizes initially show akin performance without convective flow. With the enhancement of sunlight, the realized evaporation rate of ~2.5 kg m^{-2} h^{-1} is larger than that under the dark condition of ~0.4 kg m^{-2} h^{-1}. This is also higher than the theoretical value of 2D evaporator (1.5–1.6 kg m^{-2} h^{-1}),[20,42] which can be attributed to the energy harvest from the environment (Figure S8).[20,24,43]

Again, it is clear that the 3D IPCFs with a larger pore size (~1 mm) realize higher evaporation rates compared with the ones with smaller pore size (~100 μm). For instance, under 1-sun illumination coupled with convective flows of 2 and 6 m s^{-1}, the evaporative performances of the 3D IPCF with averaged pore size of 5.8 mm are 7.8 and 10.9 kg m^{-2} h^{-1}, respectively, higher than those of the 3D IPCF with a

Please cite this article in press as: Li et al., Over 10 kg m^{-2} h^{-1} Evaporation Rate Enabled by a 3D Interconnected Porous Carbon Foam, Joule (2020), https://doi.org/10.1016/j.joule.2020.02.014

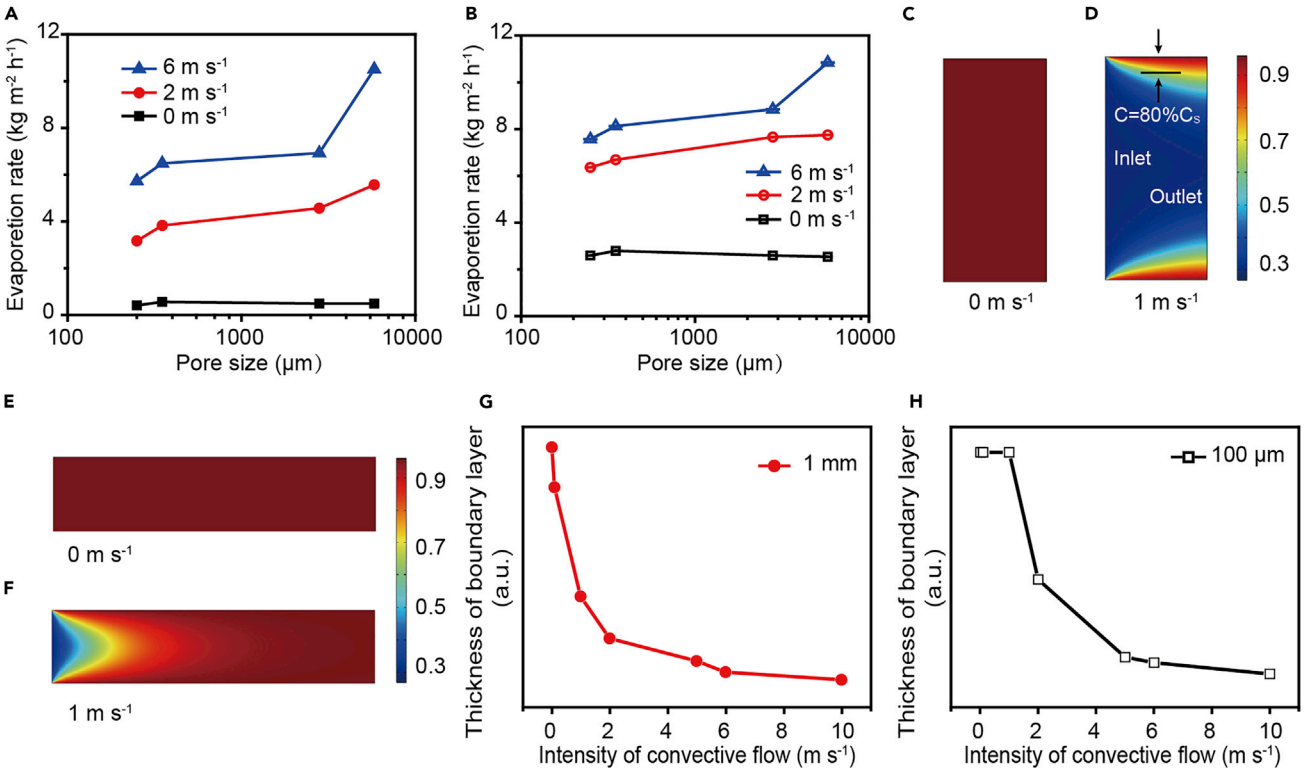

Figure 3. Relationships between Evaporative Performance and Pore Size of the 3D IPCF

(A) The dependence of evaporation rates of the 3D IPCF on pore size with various convection flows (without sunlight illumination). Evaporators with large pores enable more effective vapor diffusion, thus realizing higher evaporation rates.

(B) The dependence of evaporation rates of the 3D IPCF on pore size with various convective flows under 1-sun illumination.

(C–F) Distributions of vapor concentration in micropores with different convective flows (0 and 1 m s^{-1}). The pore diameter is 1 mm for (C) and (D) and 100 μm for (E) and (F). The lengths of these pores are set to be 400 μm.

(G and H) Dependence of the thickness of the boundary layer on the incoming convective flow for pore diameters of 1 mm (G) and 100 μm (H). The faster decrease in thickness of the boundary layer suggests intensified vapor diffusion for the evaporator with larger pores.

mean pore size of 150 μm (6.4 kg m^{-2} h^{-1} with 2 m s^{-1} and 7.6 kg m^{-2} h^{-1} with 6 m s^{-1}, respectively). It is expected that there still has a huge potential for future improvement (see Supplemental Experimental Procedures).

The microscopic mechanism of dependence of the evaporation rate on pore size is revealed by a theoretical model (see Supplemental Experimental Procedures). In this model, two typical pores with diameters of 1 mm and 100 μm (both 400 μm in length) are studied. Convective flows pass through the 1D micropores from left. The upper and lower walls of these pores are evaporative surfaces. As shown in Figures 3C and 3D, after introducing a slight convective flow, the fields of vapor concentrations for the upper and lower wall (1 mm pore) evolve from severe interference (insufficient diffusion of vapor) to complete noninterference (full diffusion of vapor). However, for the pore with a smaller diameter (100 μm), the interference of two walls still exists under the same convective flow (Figures 3E and 3F), indicating weak diffusion of vapor.

To quantitatively reflect the intensity of vapor diffusion, and the heat and mass transfer between evaporative wall and convective flow, we define the thickness of boundary layer as the distance between the evaporative wall and the point where its vapor concentration is 80% of the saturated vapor concentration (Figure 3D).[35–37,44] It is clear that the thickness of the boundary layer for the larger pore (Figure 3G)

Please cite this article in press as: Li et al., Over 10 kg m^{-2} h^{-1} Evaporation Rate Enabled by a 3D Interconnected Porous Carbon Foam, Joule (2020), https://doi.org/10.1016/j.joule.2020.02.014

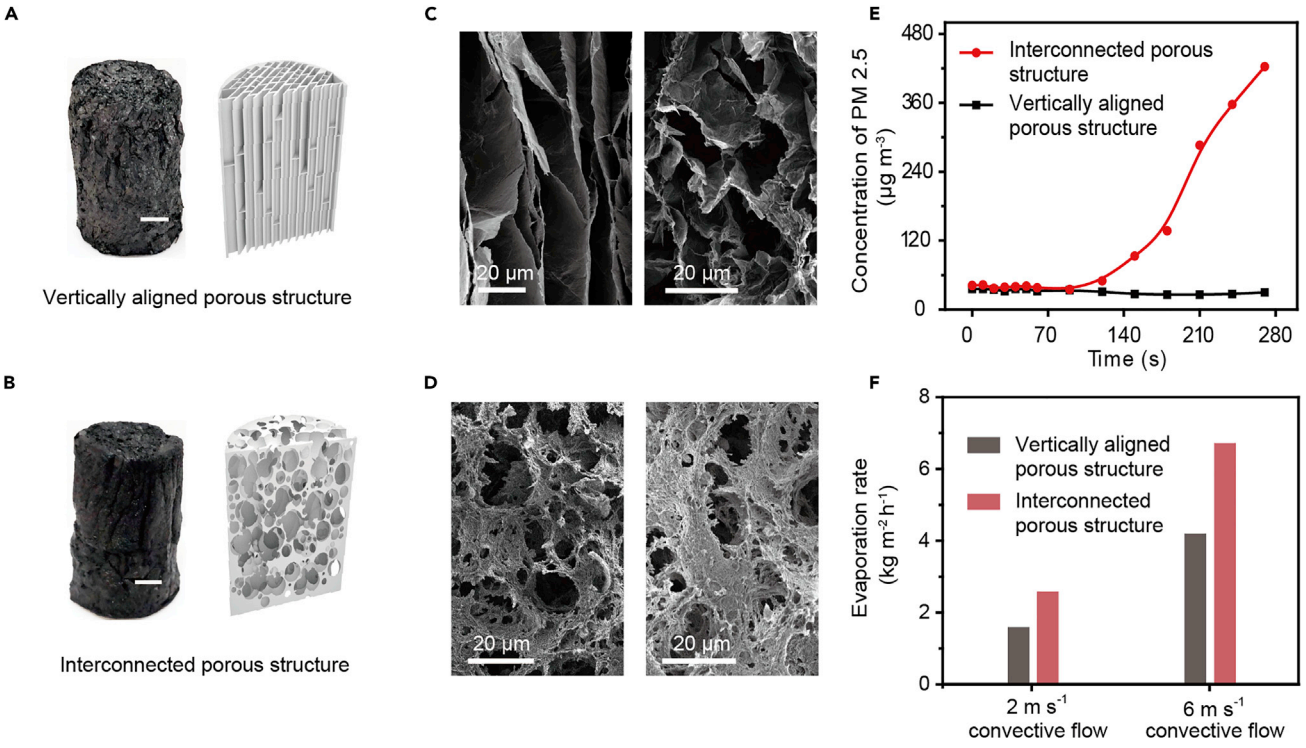

Figure 4. Correlation between the Morphology of Porous Structure and Evaporative Performance

(A and B) 3D aerogels with two kinds of porous morphologies. (A) Vertically aligned porous structure and (B) interconnected porous structure (preferred) were used for comparison. Optical images (left panel) and schematics (right panel). Scale bar, 1 cm.

(C and D) SEM images of 3D aerogel with a vertically aligned porous structure and the one with an interconnected porous structure, respectively. The left panels of (C) and (D) are cross-section views. The right panels show bird's views.

(E) PM2.5 permeability of the vertically aligned porous structure and the interconnected porous structure.

(F) Evaporation rates of the 3D aerogel with two different morphologies assisted with convective flows of 2 and 6 m s^{-1}. The interconnected porous one evaporates much faster than the vertically aligned one.

decreases much faster than that of the smaller one (Figure 3H), suggesting an intensified vapor diffusion in the larger pore (see Figure S9 for more information). These results match well with the experimental results shown above.

Relationship between Performance and Pore Morphology

Besides pore size, the morphology of porous structure also plays a vital role in utilizing the incoming convective flow to accelerate vapor diffusion. To reveal the correlation between pore morphology and evaporative performance, we developed 3D aerogels with two kinds of porous morphologies, a vertically aligned porous structure (Figure 4A) and an interconnected porous structure (Figure 4B). The mean pore sizes of these two kinds are intentionally to be kept similar (~8 μm, see Figure S10 for distributions). The scanning electron microscopy (SEM) image of the former (Figure 4C) shows that it is composed of vertically aligned graphene oxide (GO) sheets, which have a closed end in the horizontal direction and therefore block convective flow. In contrast, the latter is composed of interconnected porous GO sheets (Figure 4D). Convective flow is able to penetrate this aerogel via its interlinked pores. These surmises are confirmed by their very different permeability of PM2.5, as shown in Figure 4E.

From Figure 4F, it is found that the evaporation rates of the 3D aerogel with interconnected porous structures are consistently larger than those of the vertically aligned porous ones, with different convective flows (2 and 6 m s^{-1}). Therefore, it is

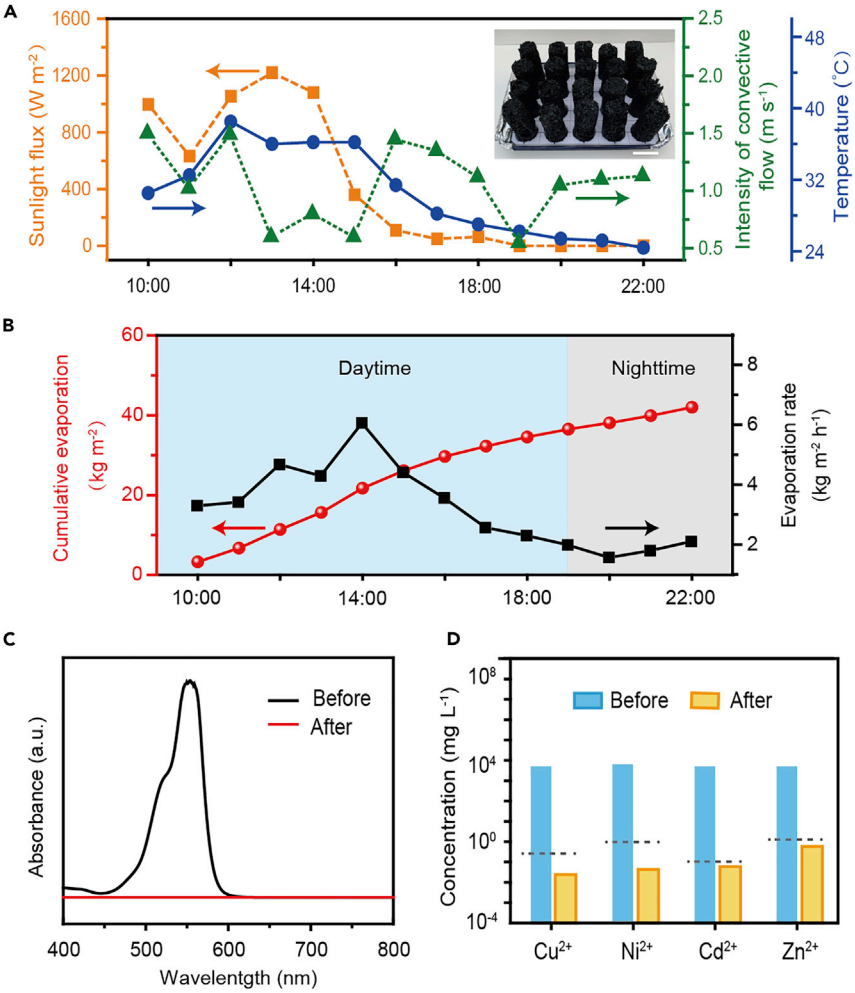

Figure 5. Outdoor Performance of the 3D IPCFs and Wastewater Treatment

(A) Outdoor conditions for evaporation: incident sunlight flux, intensity of natural convective flow, and ambient temperature over time. The incident angle of sunlight at midday is ~37°. The inset shows the setup of the large-scale device. Scale bar, 5 cm.

(B) Cumulative evaporation of the 13-h test and evaporation rate of each hour during daytime and nighttime. Assisted by a convective flow, the 3D IPCFs enable evaporation not only at daytime but also during the night.

(C and D) The 3D IPCF with an extra-high evaporation rate has direct implications in treating wastewater. (C) After water treatment, the dye molecule concentration in the vapor is undetectable (<2 μmol L^{-1}). (D) The contaminated water by heavy metal ions can be purified to the level meeting the standard of environmentally friendly discharge (the dark dash lines).

confirmed that for developing evaporators to realize a high evaporation rate, it is quite crucial to make sure the porous structures of evaporators are interconnected.

Outdoor Performance and Wastewater Treatment

To assess the evaporative performance of the 3D IPCF for practical applications, a large-scale device, composed of 20 discrete 3D IPCFs (inset of Figure 5A) was placed on the roof of Science Building at Nanjing University for outdoor tests. The corresponding incident sunlight flux, intensity of natural convective flow, and ambient temperature are recorded and summarized in Figure 5A. As shown in Figure 5B, this device achieves an accumulative evaporation of 42.0 kg m^{-2} from 9:00 a.m. to 10:00 p.m., demonstrating its high evaporative performance and great potential

Please cite this article in press as: Li et al., Over 10 kg m^{-2} h^{-1} Evaporation Rate Enabled by a 3D Interconnected Porous Carbon Foam, Joule (2020), https://doi.org/10.1016/j.joule.2020.02.014

for practical applications. Also, the evaporation rates of the large-scale device fluctuate from 2.3 to 6.1 kg m^{-2} h^{-1} at daytime and between 1.6 and 2.1 kg m^{-2} h^{-1} at night. The difference can be attributed to the variability of outdoor conditions at different periods. Therefore, it is clear that the 3D IPCFs enable high evaporation rates at both daytime and nighttime, which is desirable for practical applications.

With such a high evaporation rate, the 3D IPCF shows excellent promise in wastewater disposal. As two typical examples, the 3D IPCF was used to treat wastewater contaminated by dye molecular and heavy metal ions. Figure 5C shows that the purification enabled by the 3D IPCF evaporator can significantly reduce the concentration of dye molecular from 1 mmol L^{-1} to the level of undetectable (<2 μmol L^{-1}). Moreover, as shown in Figure 5D, the industrial wastewater with four heavy metal ions Cu^{2+} (5 g L^{-1}), Ni^{2+} (5 g L^{-1}), Cd^{2+} (5 g L^{-1}), and Zn^{2+} (5 g L^{-1}), can be purified to 0.5, 1, 0.1, and 2 mg L^{-1}, respectively, meeting the requirements of environmental protection.[45] As presented in Figure S11, the evaporation rate of the 3D IPCF stays stable during 15 cycles, showing its durability (more information in the Supplemental Experimental Procedures). It is worthy to mention that the clean vapor is discharged directly into the environment without any collection.

EXPERIMENTAL PROCEDURES

Fabrication of Three-Dimensional Interconnected Porous Carbon Foam

First, 20–30 g sucrose was added in a quartz mold (diameter of 4 cm and height of 9 cm). Subsequently, 15 mL of concentrated sulfuric acid was added in this quartz mold. After stirring them up, some of the outlets of the quartz molds were sealed by weight (~2.5 kg) for obtaining the 3D IPCFs with small pores, while free expansion without seal was adopted for fabricating 3D IPCFs with larger pores. The as-prepared samples (with a height of 9–17 cm) were cut into the desired size with a diameter of ~4 cm and a height of 6 cm. In this process, we intentionally chose the parts with the desired gradients and measured their average pore size.

Fabrication of Evaporators for Comparison

The 3D aerogels were fabricated through successive hydrothermal reaction, liquid nitrogen freezing, and freeze-drying. First, the homogeneous dispersion of graphene oxide (GO) aqueous with a concentration of 3 mg mL^{-1} was sealed in a Teflon-lined autoclave and maintained at 160°C. After being naturally cooled to room temperature, the cylindrical hydrogels were frozen by liquid nitrogen for 2 h. In this process, to obtain the 3D aerogel with a vertically aligned porous structure, they were wrapped tightly with foam, leaving only the bottom in contact with liquid nitrogen. For fabricating the 3D aerogel with an interconnected porous structure, its surfaces were all warped by tinfoil. Finally, the aerogels were obtained by subliming the ice crystals in samples via freeze-drying (−30°C, 5 Pa).[12,46–49]

Experiments of Indoor Evaporation

All indoor evaporative tests were performed under a temperature of 20°C ± 1°C and humidity of 47% ± 3% RH unless there are specifications. The mass change of water was recorded in real time by a high-accuracy electronic balance (FA 2004, 0.1 mg in accuracy), which was later used to determine the evaporation rate. The convective flow was provided by an electric fan. Its intensity was monitored by a hot-wire anemometers (AR866, AMART). The average intensity of convective flow on the evaporator was monitored ~1 cm in front of the evaporator. Evaporative experiments under sunlight were carried out under a solar simulator (94043A, NEWPORT) equipped with an optical filter for the standard AM 1.5 G spectrum. The incident intensity of sunlight was measured by a thermopile sensor (PowerMax-USB PM 30, COHERENT).

Materials Characterizations

The XPS spectrum was measured by a PHI 5000 Versa Probe, attached with a monochromatic Al Ka X-ray source. A surface tension-contact angle meter (GBX Digidrop) was used to characterize the wettability of the 3D IPCF. The microstructures were characterized by an optical microscope (DS-FI2, Nikon) and an SEM (FEI, Quanta 200). The absorption spectrum of 3D IPCF was measured by a ultraviolet-visible (UV-vis) spectroscopy (UV-360, SHIMADZU), equipped with an integrating sphere (ISR-310). The concentrations of rhodamine B and cations in water samples before and after purification were monitored via the aforementioned UV-vis spectroscopy and ICP-OES (PerkinElmer Instruments, PTIMA 5300 DV), respectively.

SUPPLEMENTAL INFORMATION

Supplemental Information can be found online at https://doi.org/10.1016/j.joule.2020.02.014.

ACKNOWLEDGMENTS

We acknowledge the micro-fabrication center of National Laboratory of Solid State Microstructures (NLSSM) for technical support. This work is jointly supported by the National Key Research and Development Program of China (no. 2017YFA0205700), National Natural Science Foundation of China (no. 21805132, 11574143, 11874211, 11621091, and 61735008), Natural Science Foundation of Jiangsu Province (no. BK20180341) and the Fundamental Research Funds for the Central Universities (no. 021314380150, 021314380140).

AUTHOR CONTRIBUTIONS

J. Li, X.W., and J. Zhu designed experiments. J. Zhu, L. Zhou, and S. Zhu supervised the project. Z. Lin and G. Liu built the theoretical model. J. Li, X.W., N.X., X.Li., J. Liang, W. Zhao, R. Lin, and B. Zhu performed experiments. All authors discussed experiments and results. J. Li, X.W., Z. Lin, and J. Zhu prepared and revised the manuscript.

DECLARATION OF INTERESTS

The authors declare no competing interests.

Received: December 6, 2019
Revised: January 28, 2020
Accepted: February 28, 2020
Published: March 25, 2020

REFERENCES

1. Mekonnen, M.M., and Hoekstra, A.Y. (2016). Four billion people facing severe water scarcity. Sci. Adv. *2*, e1500323.

2. Jassby, D., Cath, T.Y., and Buisson, H. (2018). The role of nanotechnology in industrial water treatment. Nat. Nanotechnol. *13*, 670–672.

3. Alvarez, P.J.J., Chan, C.K., Elimelech, M., Halas, N.J., and Villagrán, D. (2018). Emerging opportunities for nanotechnology to enhance water security. Nat. Nanotechnol. *13*, 634–641.

4. United Nations (2019). The United Nations world water development report 2019. United Nations. https://www.unwater.org/publications/world-water-development-report-2019/.

5. Mauter, M.S., Zucker, I., Perreault, F., Werber, J.R., Kim, J., and Elimelech, M. (2018). The role of nanotechnology in tackling global water challenges. Nat. Sustain. *1*, 166–175.

6. Tong, T., and Elimelech, M. (2016). The global rise of zero liquid discharge for wastewater management: drivers, technologies, and future directions. Environ. Sci. Technol. *50*, 6846–6855.

7. Chen, C., Kuang, Y., and Hu, L. (2019). Challenges and opportunities for solar evaporation. Joule *3*, 683–718.

8. Zhang, P., Liao, Q., Yao, H., Huang, Y., Cheng, H., and Qu, L. (2019). Direct solar steam generation system for clean water production. Energy Storage Mater. *18*, 429–446.

9. Zhou, L., Tan, Y., Wang, J., Xu, W., Yuan, Y., Cai, W., Zhu, S., and Zhu, J. (2016). 3D self-assembly of aluminum nanoparticles for plasmon enhanced solar desalination. Nat. Photonics *10*, 393–398.

10. Geng, H., Xu, Q., Wu, M., Ma, H., Zhang, P., Gao, T., Qu, L., Ma, T., and Li, C. (2019). Plant leaves inspired sunlight-driven purifier for high-efficiency clean water production. Nat. Commun. *10*, 1512.

11. Ren, H., Tang, M., Guan, B., Wang, K., Yang, J., Wang, F., Wang, M., Shan, J., Chen, Z., Wei, D., et al. (2017). Hierarchical graphene foam for efficient omnidirectional solar–thermal energy conversion. Adv. Mater. *29*, 1702590.

12. Yang, Y., Zhao, R., Zhang, T., Zhao, K., Xiao, P., Ma, Y., Ajayan, P.M., Shi, G., and Chen, Y. (2018). Graphene-based standalone solar energy converter for water desalination and purification. ACS Nano *12*, 829–835.

13. Shi, Y., Zhang, C., Li, R., Zhuo, S., Jin, Y., Shi, L., Hong, S., Chang, J., Ong, C., and Wang, P. (2018). Solar evaporator with controlled salt precipitation for zero liquid discharge desalination. Environ. Sci. Technol. *52*, 11822–11830.

14. Finnerty, C., Zhang, L., Sedlak, D.L., Nelson, K.L., and Mi, B. (2017). Synthetic graphene oxide leaf for solar desalination with zero liquid discharge. Environ. Sci. Technol. *51*, 11701–11709.

15. Kuang, Y., Chen, C., He, S., Hitz, E.M., Wang, Y., Gan, W., Mi, R., and Hu, L. (2019). A high-performance self-regenerating solar evaporator for continuous water desalination. Adv. Mater. *29*, 1900498.

16. Neumann, O., Feronti, C., Neumann, A.D., Dong, A., Schell, K., Lu, B., Kim, E., Quinn, M., Thompson, S., Grady, N., et al. (2013). Compact solar autoclave based on steam generation using broadband light-harvesting nanoparticles. Proc. Natl. Acad. Sci. U S A *110*, 11677–11681.

17. Liu, F., Zhao, B., Wu, W., Yang, H., Ning, Y., Lai, Y., and Bradley, R. (2018). Low cost, robust, environmentally friendly geopolymer–mesoporous carbon composites for efficient solar powered steam generation. Adv. Funct. Mater. *28*, 1803266.

18. Cui, L., Zhang, P., Xiao, Y., Liang, Y., Liang, H., Cheng, Z., and Qu, L. (2018). High rate production of clean water based on the combined photo-electro-thermal effect of graphene architecture. Adv. Mater. *30*, e1706805.

19. Li, Z., Wang, C., Su, J., Ling, S., Wang, W., and An, M. (2019). Fast-growing field of interfacial solar steam generation: evolutional materials, engineered architectures, and synergistic applications. Sol. RRL *3*, 1800206.

20. Li, X., Li, J., Lu, J., Xu, N., Chen, C., Min, X., Zhu, B., Li, H., Zhou, L., Zhu, S., et al. (2018). Enhancement of interfacial solar vapor generation by environmental energy. Joule *2*, 1331–1338.

21. Xu, N., Li, J., Wang, Y., Fang, C., Li, X., Wang, Y., Zhou, L., Zhu, B., Wu, Z., Zhu, S., et al. (2019). A water lily–inspired hierarchical design for stable and efficient solar evaporation of high-salinity brine. Sci. Adv. *5*, eaaw7013.

22. Li, W., Li, Z., Bertelsmann, K., and Fan, D.E. (2019). Portable low-pressure solar steaming-collection unisystem with polypyrrole origamis. Adv. Mater. *31*, e1900720.

23. Li, W., Tekell, M.C., Huang, Y., Bertelsmann, K., Lau, M., and Fan, D. (2018). Synergistic high-rate solar steaming and mercury removal with MoS2/C@ Polyurethane composite sponges. Adv. Energy Mater. *8*, 1802108.

24. Shi, Y., Li, R., Jin, Y., Zhuo, S., Shi, L., Chang, J., Hong, S., Ng, K., and Wang, P. (2018). A 3D photothermal structure toward improved energy efficiency in solar steam generation. Joule *2*, 1171–1186.

25. Sun, Z., Wang, J., Wu, Q., Wang, Z., Wang, Z., Sun, J., and Liu, C. (2019). Plasmon based double-layer hydrogel device for a highly efficient solar vapor generation. Adv. Funct. Mater. *29*, 1901312.

26. Xia, Y., Hou, Q., Jubaer, H., Li, Y., Kang, Y., Yuan, S., Liu, H., Woo, M.W., Zhang, L., Gao, L., et al. (2019). Spatially isolating salt crystallisation from water evaporation for continuous solar steam generation and salt harvesting. Energy Environ. Sci. *12*, 1840–1847.

27. Ni, G., Li, G., Boriskina, S.V., Li, H., Yang, W., Zhang, T., and Chen, G. (2016). Steam generation under one sun enabled by a floating structure with thermal concentration. Nat. Energy *1*, 126.

28. Xu, W., Xing, Y., Liu, J., Wu, H., Cui, Y., Li, D., Guo, D., Li, C., Liu, A., and Bai, H. (2019). Efficient water transport and solar steam generation via radially, hierarchically structured aerogels. ACS Nano *13*, 7930–7938.

29. Gao, M., Zhu, L., Peh, C.K., and Ho, G.W. (2019). Solar absorber material and system designs for photothermal water vaporization towards clean water and energy production. Energy Environ. Sci. *12*, 841–864.

30. Li, Y., Gao, T., Yang, Z., Chen, C., Luo, W., Song, J., Hitz, E., Jia, C., Zhou, Y., Liu, B., et al. (2017). 3D-printed, all-in-one evaporator for high-efficiency solar steam generation under 1 sun illumination. Adv. Mater. *29*, 28470982.

31. Zhu, L., Gao, M., Peh, C.K.N., Wang, X., and Ho, G.W. (2018). Self-contained monolithic carbon sponges for solar-driven interfacial water evaporation distillation and electricity generation. Adv. Energy Mater. *8*, 1702149.

32. Zhou, X., Zhao, F., Guo, Y., Zhang, Y., and Yu, G. (2018). A hydrogel-based antifouling solar evaporator for highly efficient water desalination. Energy Environ. Sci. *11*, 1985–1992.

33. Zhou, L., Tan, Y., Ji, D., Zhu, B., Zhang, P., Xu, J., Gan, Q., Yu, Z., and Zhu, J. (2016). Self-assembly of highly efficient, broadband plasmonic absorbers for solar steam generation. Sci. Adv. *2*, e1501227.

34. Yiotis, A.G., Tsimpanogiannis, I.N., Stubos, A.K., and Yortsos, Y.C. (2007). Coupling between external and internal mass transfer during drying of a porous medium. Water Resour. Res. *43*, W06403.

35. Shahraeeni, E., Lehmann, P., and Or, D. (2012). Coupling of evaporative fluxes from drying porous surfaces with air boundary layer: characteristics of evaporation from discrete pores. Water Resour. Res. *48*, W09525.

36. Moran, M.J., Shapiro, H.N., Boettner, D.D., and Bailey, M.B. (2010). Fundamentals of Engineering Thermodynamics (John Wiley & Sons).

37. Bergman, T.L., Incropera, F.P., DeWitt, D.P., and Lavine, A.S. (2011). Fundamentals of Heat and Mass Transfer (John Wiley & Sons).

38. Zhou, L., Li, X., Ni, G.W., Zhu, S., and Zhu, J. (2019). The revival of thermal utilization from the sun: interfacial solar vapor generation. Natl. Sci. Rev. *6*, 562–578.

39. The American Society for Testing and Materials (2012). Standard tables for reference solar spectral irradiances: direct normal and hemispherical on 37° tilted surface (ASTM). https://www.astm.org/Standards/G173.htm.

40. Shrotriya, V., Li, G., Yao, Y., Moriarty, T., Emery, K., and Yang, Y. (2006). Accurate measurement and characterization of organic solar cells. Adv. Funct. Mater. *16*, 2016–2023.

41. National Weather Service. Beaufort Wind Scale. National weather service. https://www.weather.gov/mfl/beaufort.

42. Service Robert, F. (2019). New solar technology could produce clean drinking water for millions in need. Science. https://www.sciencemag.org/news/2019/06/new-solar-technology-could-produce-clean-drinking-water-millions-need.

43. Song, H., Liu, Y., Liu, Z., Singer, M.H., Li, C., Cheney, A.R., Ji, D., Zhou, L., Zhang, N., Zeng, X., et al. (2018). Cold vapor generation beyond the input solar energy limit. Adv. Sci. *5*, 1800222.

44. Sinaiski, E.G. (2011). Hydromechanics: Theory and Fundamentals (John Wiley & Sons).

45. Ministry of Ecology and Environment of The People's Republic of China. Emission standard of pollutants for copper, nickel, cobalt industry. Ministry of Ecology and Environment of The People's Republic of China, accessed 22 September 2019. http://bz.mee.gov.cn/bzwb/shjbh/swrwpfbz/201010/W020130129576197714454.pdf.

46. Sheng, K., Xu, Y., Li, C., and Shi, G. (2011). High-performance self-assembled graphene hydrogels prepared by chemical reduction of graphene oxide. New Carbon Mater. *26*, 9–15.

47. Zhang, P., Li, J., Lv, L., Zhao, Y., and Qu, L. (2017). Vertically aligned graphene sheets membrane for highly efficient solar thermal generation of clean water. ACS Nano *11*, 5087–5093.

48. Min, P., Liu, J., Li, X., An, F., Liu, P., Shen, Y., Koratkar, N., and Yu, Z. (2018). Thermally conductive phase change composites featuring anisotropic graphene aerogels for real-time and fast-charging solar-thermal energy conversion. Adv. Funct. Mater. *28*, 1805365.

49. Hu, X., Xu, W., Zhou, L., Tan, Y., Wang, Y., Zhu, S., and Zhu, J. (2017). Tailoring graphene oxide-based aerogels for efficient solar steam generation under one sun. Adv. Mater. *29*, 27885728.